

Article

Reactive Magnetron Sputter Deposition of Bismuth Tungstate Coatings for Water Treatment Applications under Natural Sunlight

Marina Ratova ^{1,*}, Rafaela B. P. Marcelino ² , Patterson P. de Souza ³, Camila C. Amorim ² and Peter J. Kelly ¹ 

¹ Surface Engineering Group, School of Engineering, Manchester Metropolitan University, Manchester M1 5GD, UK; peter.kelly@mmu.ac.uk

² Department of Sanitary and Environmental Engineering, Universidade Federal de Minas Gerais, 6627 Av. Antônio Carlos, Bairro Pampulha, Belo Horizonte-MG 31270-901, Brazil; rafaelaportela@gmail.com (R.B.P.M.); camila@desa.ufmg.br (C.C.A.)

³ Department of Chemistry, Centro Federal de Educação Tecnológica de Minas Gerais, Av. Amazonas 5253, Belo Horizonte 30431-025, Brazil; patterson@cefetmg.br

* Correspondence: marina_ratova@hotmail.com; Tel.: +44-161-247-4648

Received: 8 September 2017; Accepted: 21 September 2017; Published: 23 September 2017

Abstract: Bismuth complex oxides, in particular, bismuth tungstate, have recently attracted attention as promising photocatalytic materials for water treatment processes. In the present work, photocatalytic bismuth tungstate films were prepared by pulsed direct current (DC) reactive magnetron sputtering of Bi and W targets in an Ar/O₂ atmosphere onto spherically-shaped glass beads. The uniform coverage of the substrate was enabled by the use of oscillating bowl placed underneath the magnetrons. The atomic ratio of Bi/W was varied through the variation of the power applied to the magnetrons. The deposited coatings were analyzed by the scanning electron microscopy (SEM), energy dispersive X-ray spectroscopy (EDX), X-ray diffraction (XRD), X-ray photoelectron spectroscopy and atomic force microscopy. The photocatalytic properties of the films were studied via the methylene blue (MB) degradation process under artificial (fluorescent light) and natural (sunlight) irradiation, and compared to the photocatalytic performance of titanium dioxide coatings deposited onto identical substrates. The results showed that the photocatalytic performance of bismuth tungstate and bismuth oxide-coated beads was superior to that exhibited by TiO₂-coated beads. Overall, reactive magnetron co-sputtering has been shown to be a promising technique for deposition of narrow band gap bismuth-based semiconducting oxides onto irregularly-shaped substrates for potential use in water treatment applications.

Keywords: bismuth tungstate; titanium dioxide; photocatalysis; magnetron sputtering; water treatment; solar irradiance

1. Introduction

Since the discovery of the photocatalytic phenomenon in 1969 [1], it has become the subject of extensive research work, and proposed as a promising and sustainable method for decontamination of air, water and soil [2,3]. In particular, photocatalytic purification of wastewater is becoming an increasingly popular process, with a number of reviews published in the past few years [4–6]. A wide range of titanium dioxide-based materials have been successfully applied as photocatalysts for water treatment [7–9]. However, most of the authors note that the use of semiconductor photocatalysis for the treatment of water is restricted by several major factors. Firstly, titanium dioxide, as the most widely available and studied photocatalytic material, is typically characterized with a relatively high

band gap value (3.2 eV for anatase phase) and low photonic efficiency due to fast recombination of the photogenerated electrons and holes. The high band gap value results in titania photocatalysts being activated only with ultraviolet (UV) irradiation (less than 5% of the solar spectrum), therefore, for practical use, additional irradiation sources are required. Consequently, it is rather difficult to achieve high reaction rates, as required when dealing with heavily-polluted industrial wastewater or high throughput systems. Secondly, the choice of the physical form of the photocatalyst to be used represents a complicated task, as both powdered photocatalysts and those in the form of thin films have their own disadvantages. Thus, the use of a photocatalyst in powdered form results in high surface area, but presents significant difficulties in recovering the powder from the treated water. On the other hand, photocatalytic coatings deposited onto flat substrates do not require complicated recovery, however they are characterized with low surface area values, compared to powdered photocatalysts and are, therefore, not suitable for high-throughput processes.

As photocatalytic wastewater treatment is aimed at being an economical and practical technique, it is desirable to avoid the extra costs of using artificial light sources in the photocatalytic treatment setup. Use of natural sunlight represents a cheap and sustainable irradiation source, however, as in the case of titania-based photocatalysts, its efficiency can be rather low. In addition to that, most of the reports lack data on the use of natural sunlight as an irradiation source for the photocatalytic materials studied. Therefore, summarizing all the above, to provide an efficient and environmentally-friendly solution for water treatment, there is an obvious need for the development of photocatalytic materials based on the use of low band gap semiconductors, combining visible light activity with high photonic efficiency and high surface area. The development of such a photocatalyst is also an urgent need from the view point of using solar energy, rather than artificial irradiation sources.

In recent years the subject of using novel visible light-activated narrow band gap photocatalytic materials has become increasingly popular. Binary metal oxides, such as ZnO, CdS, Fe₂O₃, and WO₃, have been extensively tested, however each has their own disadvantages, limiting their practical use as an efficient alternative to TiO₂ [10]. Bismuth complex oxides have recently attracted researchers' attention as promising candidates for visible light photocatalysis due to the fact that they are typically characterized with low band gap values, as the result of the hybridization between the Bi 2*p* and O 2*s* states [11]. Bismuth tungstate, Bi₂WO₆, is one of the most widely studied and reportedly efficient photocatalytic materials [12–16]. However, there are very few reports to date describing the use of bismuth tungstate for water purification [17,18].

Magnetron sputtering represents a relatively simple, versatile, and readily scalable method for the deposition of thin functional films onto a variety of substrates [19]. As the substrates can range in size from several mm² to 6 m × 3 m “jumbo” sheets of architectural glazing, the deposition process is widely used for the production of various coatings, including photocatalysts, both in laboratory and industrial facilities. However, it is generally accepted that magnetron sputtering is predominately a “line of sight” process, best suited for the deposition of coatings onto flat substrates [20]. Nevertheless, the authors have recently successfully developed and reported a technology that enables the deposition of photocatalytic coatings onto substrates of “irregular” shape, such as powders and nanoparticles [20,21]. In the present work, this process was used for the deposition of photocatalytic bismuth tungstate coatings onto spherically-shaped glass beads, as opposed to the flat substrates reported in earlier work of the authors, to provide considerably higher surface area. Bismuth tungstate coatings are often described as efficient visible light-activated photocatalytic materials [15], however, they are usually produced by chemical methods, e.g., hydrothermal methods [13,14] or electrospinning [22]. Use of photocatalyst-coated particulates is frequently reported for water treatment applications, however, chemical methods are typically used for the coating's deposition [23–25]. The establishment of a reactive sputter deposition method as a technique for the production of bismuth complex oxides [15,21,26] allows some limitations of these chemical deposition methods, such as the use of hazardous precursors or byproduct formation, to be overcome and provides a simple, yet efficient and readily up-scalable deposition technique. To the best of our knowledge, the deposition of photocatalytic bismuth tungstate

coatings via reactive magnetron sputtering onto oscillating glass beads has not been reported elsewhere to date.

Therefore, in the present study, photocatalytic bismuth tungstate coatings were deposited onto 2 mm diameter glass beads, via reactive magnetron sputtering from a dual source system (i.e., one consisting of two magnetrons). The beads were manipulated using an oscillating bowl placed under the magnetrons in order to provide uniform coverage. Photocatalytic properties of the coatings were assessed via their ability to degrade an organic dye (methylene blue) under artificial (fluorescent light) and natural (sunlight) irradiation. The photocatalytic performance of the bismuth tungstate-coated beads was compared to that of titanium dioxide coatings deposited onto identical beads.

2. Results and Discussion

2.1. Coatings Overview

An overview of deposition conditions, thickness, and compositional information of the studied coatings is presented in Table 1. Compositional data of the coatings are in good agreement with the earlier publications, as increasing the power applied to the bismuth target resulted in deposition of significantly bismuth-rich coatings, as compared to increasing the power applied to the tungsten target. This is due to the relatively high sputtering yield of bismuth, due to its polyatomic sputtering nature [27]. Composition of the coatings was evaluated with EDX at four points for each coating on a flat glass substrate, and the variation in results was not more than 2%. The mean values of the compositional data are given in Table 1. This confirms the initial suggestion that oscillation of the glass beads under a dual magnetron source allows the production of uniform coatings on the surface of the beads.

Table 1. Compositional properties and thickness of bismuth tungstate and titanium dioxide coatings deposited onto 2-mm glass beads.

Sample ID	Bi Power, W	W Power, W	Power Ratio	Bi Content, atomic %	W Content, atomic %	Atomic % Ratio	Coating Thickness, nm
Bi0	600	0	—	100	0	—	340
BiW1	300	300	1/1	73	27	2.7/1	210
BiW2	200	400	1/2	65	35	1.8/1	160
BiW3	150	450	1/3	57	43	1.3/1	130
BiW4	120	480	1/4	52	48	1.1/1	110
BiW5	100	500	1/5	44	56	1/1	100
W0	0	600	—	0	100	—	70
TiO ₂	—	—	—	—	—	—	90

Scanning electron microscopy (SEM) was used for thickness evaluation and surface imaging of the coated beads. The thickness of the coatings was measured from cross-sectional SEM images; the glass beads were crushed prior to the measurements and mounted onto carbon adhesive discs. The selected SEM images are presented in the Figure 1. As can be seen from the cross-sectional images, the coatings are fully dense with relatively smooth surfaces. The thickness of coating Bi0 was 340 nm, with the rest of the coatings being considerably thinner. As the sputter yield for bismuth is much higher than that of tungsten, unsurprisingly, the reduction of the power to the bismuth target resulted in the deposition of much thinner coatings. It should be noted that the titanium dioxide coatings, despite using two targets driven at the same total applied power (600 W) as for the bismuth/tungsten coatings, was significantly thinner due to the lower sputtering yield of titanium.

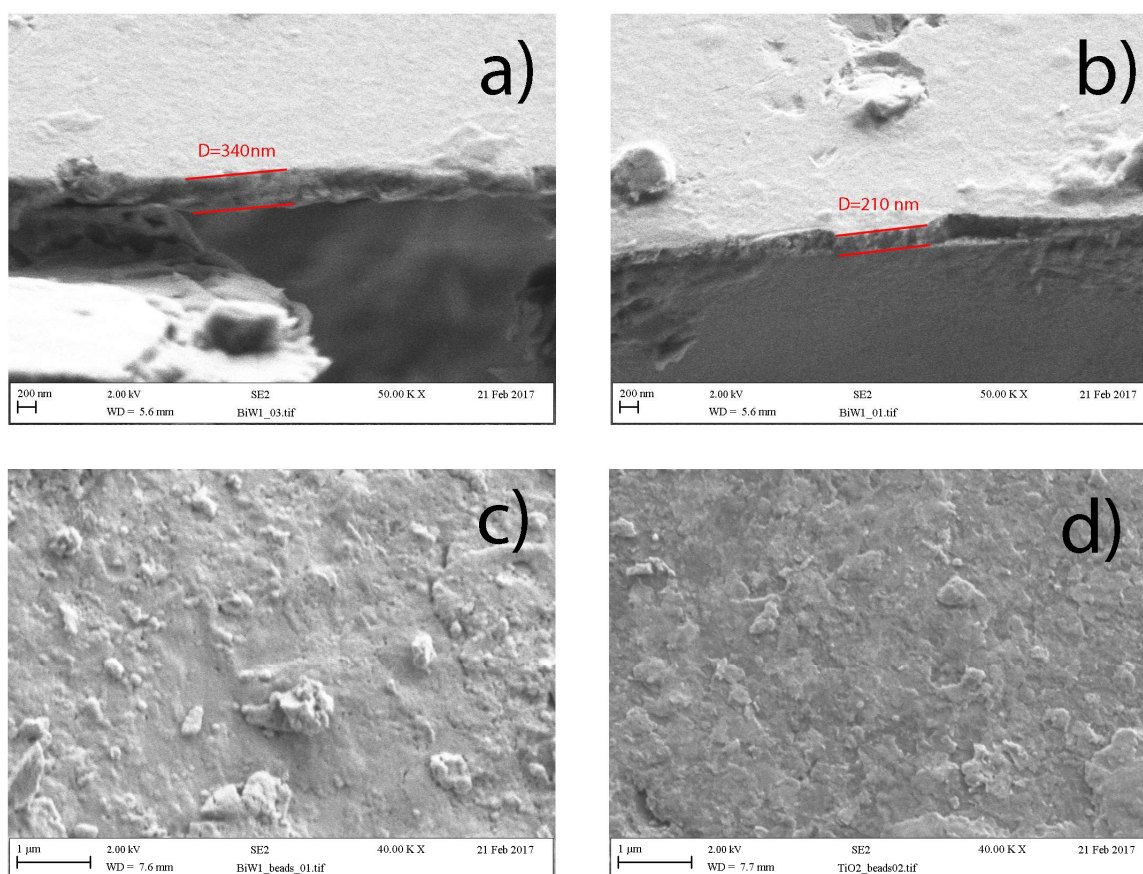


Figure 1. Cross-section SEM images of the coatings (a) Bi0, (b) BiW1 and top view SEM images of the coatings (c) BiW2, and (d) TiO₂.

Results of elemental mapping (selected mapping images are given in the Figure 2) indicated that Bi an W/Ti elements were uniformly distributed on the beads' surface.

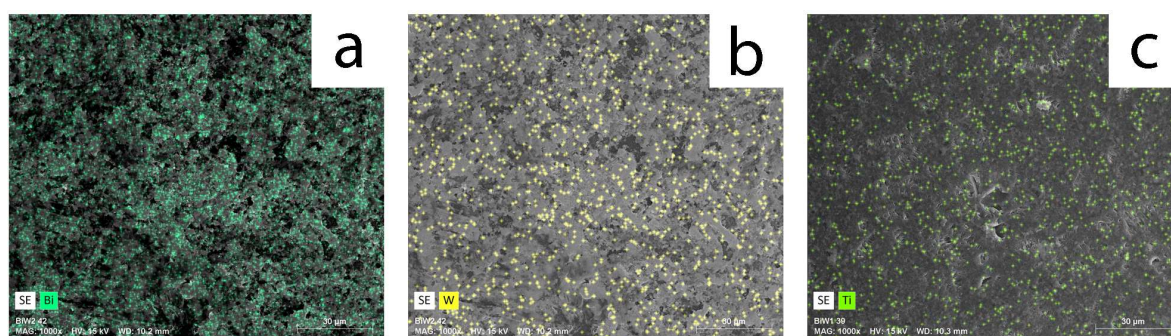


Figure 2. Results of elemental mapping for selected coatings: (a) sample BiW2 bismuth; (b) sample BiW2 tungsten; and (c) sample TiO₂ titanium.

2.2. X-Ray Diffraction (XRD) Results

The XRD results after thermal treatment of the samples are presented in the Figure 3. As evidenced from the XRD patterns, all samples, except W0, were crystalline with peaks readily observable on the patterns. Peaks seen on the pattern of sample Bi0 correspond to the bismuth oxide pattern; Bi₈O₁₂ (JCPDS 96-901-2328). As tungsten was introduced to the coatings, the peaks found on the XRD patterns

of co-sputtered samples can be attributed to various bismuth tungstate phases. Thus, all peaks on the pattern of BiW1 sample were found to belong to tetragonal russelite, with the formula $\text{Bi}_{4.5}\text{W}_{1.6}\text{O}_{16}$ (JCPDS 96-101-1216). Increasing the tungsten to bismuth ratio in the coatings resulted in changes in the composition and structure of the coatings—all peaks for both samples, BiW2 and BiW3, can be assigned to $\text{Bi}_8\text{W}_4\text{O}_{24}$ orthorhombic russelite (JCPDS 96-901-1800). In the XRD pattern of sample BiW4 $\text{Bi}_8\text{W}_4\text{O}_{24}$ peaks co-exist with the peaks attributed to the $\text{Bi}_8\text{W}_8\text{O}_{36}$ structure (JCPDS 96-721-3034), while all of the peaks of the sample BiW5 can be attributed to the latter phase. It should be noted that, despite increasing tungsten content, none of the peaks in the patterns of the co-deposited films could be attributed to tungsten oxide phases. The amorphous structure of sample W0 implies that annealing at 673 K was not sufficient to reach the crystallization point of tungsten oxide. Therefore, even tungsten-rich samples exhibited no peaks for tungsten oxides. A sample of titanium dioxide after annealing at 673 K exhibited only the peaks that could be attributed to the anatase titania phase with major peaks found at 2θ angles of 25.3° , 37.8° , 48.0° , 55.0° , and 62.6° (JCPDS 96-900-8215).

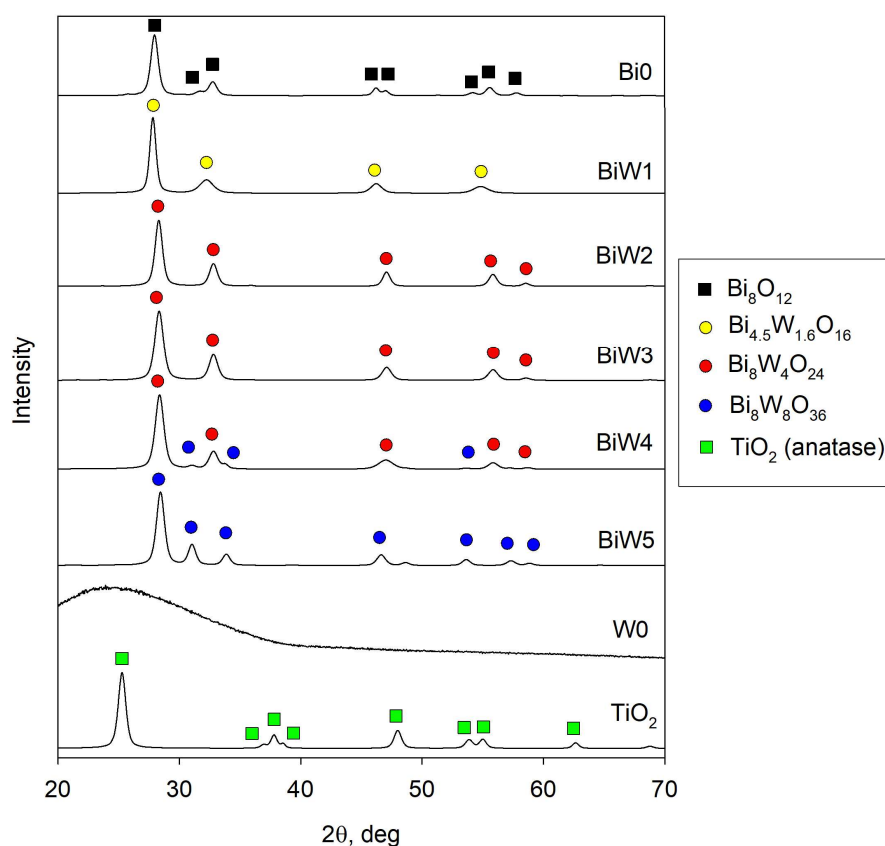


Figure 3. XRD patterns of coatings deposited onto 2-mm glass beads and annealed at 673 K.

2.3. X-Ray Photoelectron Spectroscopy (XPS) Results

Surface composition and chemical states of the elements were studied with X-ray photoelectron spectroscopy (XPS). XPS estimation of bismuth to tungsten ratios was consistent with EDX data obtained earlier. As XPS has a shallow detection depth (a few atomic layers) compared to EDX, it can be suggested that the distribution of the elements was consistent through the thickness of the coatings. Selected XPS results are presented in Figure 4. Thus, survey spectra of samples Bi0, BiW1, and TiO_2 are given in the Figure 4a,d,g, respectively. The presence of a carbon peak (C 1s peak) observed at 284.8 eV on all survey spectra is typically explained by adventitious carbon contamination; the binding energies were referenced to the adventitious carbon peak. On high resolution spectra of the samples Bi 4f peaks appeared at ca. 158.3 eV and ca. 163.6 eV (Figure 4b,e); W 4f peaks were found at ca. 34.8 and ca. 37 eV

(Figure 4f). It should be noted here that no significant shifts were observed in the positions of Bi 4f and W 4f peaks for all samples of the Bi/W array. Figure 4c,i show high-resolution spectra for O 1s binding energies, for samples Bi0 and TiO₂, respectively—two peaks can be clearly seen at ca. 529.5 and ca. 531.3 eV; these are typically attributed to metal oxide bonds and organic C–O bonds, respectively. On the high-resolution spectrum of Ti 2p (Figure 4h), the peak positioned at ca. 458.3 eV corresponds to Ti 2p_{3/2}, while the peak at ca. 464.1 eV can be assigned to Ti 2p_{1/2}. The positions of the all the peaks observed were in good agreement with the data typically reported in the literature [28,29].

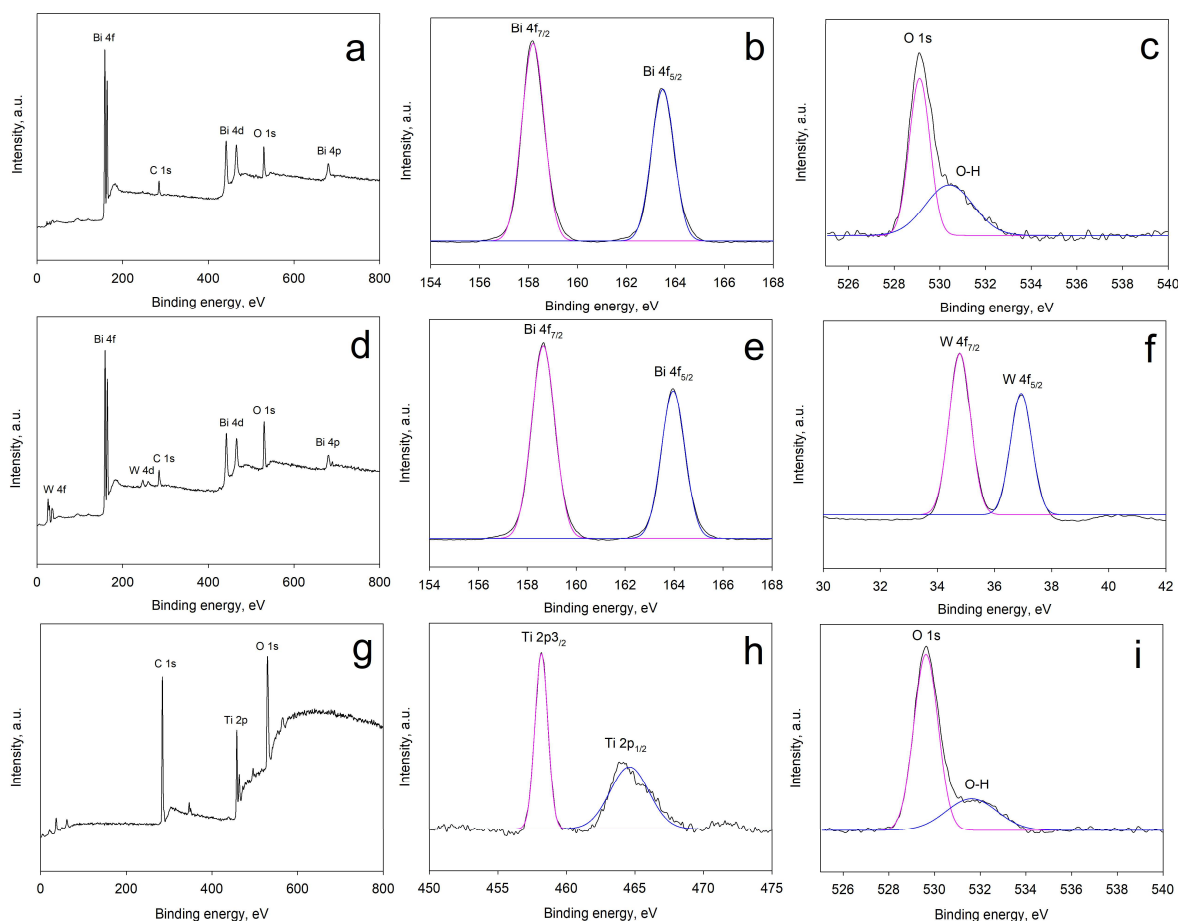


Figure 4. XPS results of 2-mm coated beads: sample Bi0 (a) survey spectrum, (b) Bi 4f spectrum, (c) O 1s spectrum; sample BiW1 (d) survey spectrum; (e) Bi 4f spectrum; (f) W 4f spectrum; sample TiO₂; (g) survey spectrum; (h) Ti 2p spectrum; and (i) O 1s spectrum.

2.4. Atomic Force Microscopy (AFM) Results

Morphological properties of the coatings were studied with atomic force microscopy (AFM). Selected AFM images are presented in the Figure 5. Values of surface roughness (R_a) and surface area (S_a) of the studied coatings obtained by AFM are given in Table 2. As can be seen from the results, all coatings were characterized with similar values of surface parameters, with the bismuth oxide coating, Bi0, being slightly rougher than the rest of the experimental array. As the surface area variation was <1% for all the coatings, their photocatalytic properties could be compared directly in this case, as the variation in photocatalytic activity of the samples cannot be attributed to the increased area of contact between the pollutant and the coating.

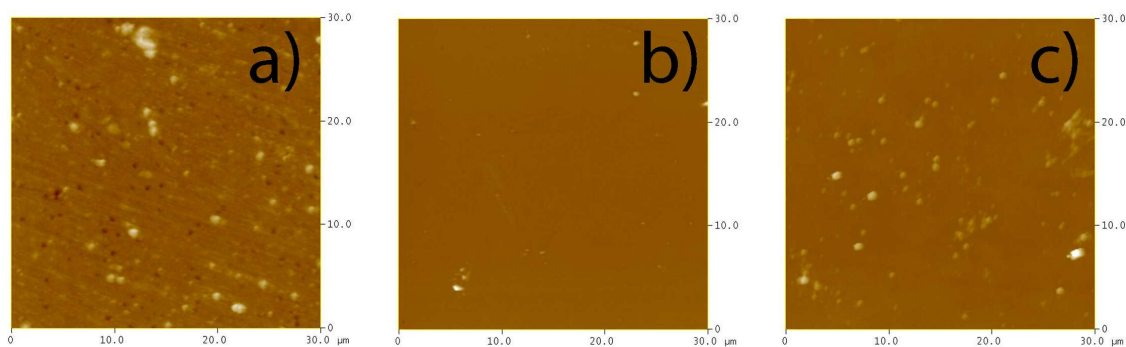


Figure 5. AFM images of selected coatings: (a) BiO; (b) BiW1; and (c) TiO₂.

Table 2. Phase, surface, optical, and photocatalytic properties of coatings deposited onto 2 mm glass beads after annealing at 673 K.

Sample ID	Major Crystal Phase	Surface Roughness R_a , nm	Surface Area S_a , μm^2	Band Gap, eV	Absorption Edge, nm
Bi0	Bismuth oxide	8.3	904	2.40	516.7
BiW1	Russelite Bi _{4.5} W _{1.6} O ₁₆	6.6	902	2.57	482.5
BiW2	Russelite Bi ₈ W ₄ O ₂₄	7.3	903	2.64	469.7
BiW3	Russelite Bi ₈ W ₄ O ₂₄	6.4	902	2.68	462.7
BiW4	Russelite Bi ₈ W ₄ O ₂₄ /bismuth tungstate Bi ₈ W ₈ O ₃₆	4.5	902	2.75	450.9
BiW5	Bismuth tungstate Bi ₈ W ₈ O ₃₆	3.8	901	2.83	438.2
W0	None (amorphous)	5.5	901	2.97	417.5
TiO ₂	Anatase	4.8	900	—	388.7

2.5. Optical Properties (Band Gap Calculation)

The classical Tauc plot method was used for estimating the optical band gaps of the deposited coatings, as described earlier in the Experimental section, assuming indirect allowed transitions [15,30]. Examples of the band gap calculation for selected coatings (BiO, BiW1, and TiO₂) are shown in Figure 6. The values of the estimated band gaps are given in Table 2. It is evident from the data given in this table that the variation of the bismuth/tungsten content had a great effect on the values of the band gap. Thus, the band gap of the bismuth oxide coating, BiO, was only 2.4 eV; introduction of tungsten to the coatings resulted in an immediate band gap broadening to a value of 2.57 eV (coating BiW1). As the content of tungsten relative to the content of bismuth increased, further band gap broadening was observed. The band gap of tungsten oxide (sample W0) was estimated as 2.97 eV. Therefore, it is obvious from the data that increasing the content of tungsten over bismuth resulted in a “blue” shift of the band gap towards the UV range. The band gap of the titanium dioxide sample was considerably higher, compared to the values obtained for the bismuth/tungsten coatings—3.2 eV. The band gap data are generally in good agreement with the literature information, where the value of anatase titania is typically reported to be around 3.2 eV, and the band gaps of bismuth tungstate range typically from 2.5–2.8 eV, depending on the phase and deposition method [14,15,30].

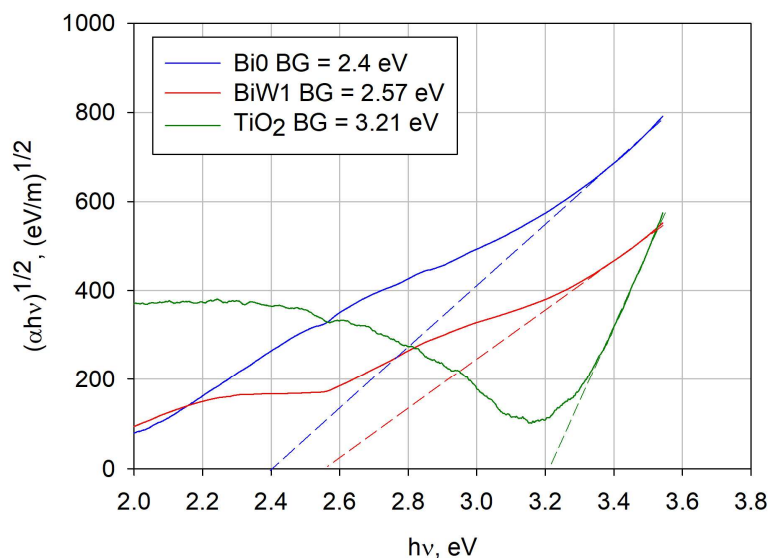


Figure 6. Examples of the band gap calculation for selected coatings: BiO, BiW1, and TiO₂.

2.6. Photocatalytic Activity Assessment

2.6.1. Indoor Assessment (Fluorescent Light Source)

The initial assessment of photocatalytic properties of the coated beads was performed in the laboratory environment via monitoring MB degradation under fluorescent light source. Despite known limitations of the MB photocatalytic test (significant non-photocatalytic photobleaching under visible light irradiation [31]), dyes, in general, and MB, in particular, are common water pollutants. Consequently, the capability of photocatalytic materials in dye degradation is important when used for water treatment applications.

Control experiments in the dark showed no decay in MB absorbance for all types of the coated beads studied. The MB absorbance decay rates for all of the samples, as well as the decay rate for photolysis (experiment with no beads), are given in the Figure 7. From the MB decay rates given it is obvious that the highest photocatalytic activity was observed for the samples BiO, BiW1, and BiW2. As the bismuth/tungsten ratio increased, the sharp drop in photocatalytic activity can be seen, with the samples BiW5 and W0 showing very low rates of MB degradation, comparable to the photolysis rate. The MB degradation rate for titanium dioxide (sample TiO₂) was lower compared to those of the most active Bi/W samples of the array, however, considerable decay still could be seen during the 1 h experiment.

These results are not surprising, as it has been shown in the earlier work that for magnetron-sputtered bismuth tungstate coatings the highest photocatalytic activity is typically achieved for the bismuth/tungsten ratio of around 2:1 [15,21], corresponding to the stoichiometric composition of Bi₂WO₆, most frequently reported as the most photocatalytically active phase. This is in good agreement with the fact that samples BiW1 and BiW2 showed higher MB degradation rates, compared to the other samples of the bismuth tungstate array. The high rate of MB degradation for bismuth oxide sample (BiO) confirms the fact that, as well as its complex oxides, Bi_xO_y is frequently reported as a photocatalytic material [32,33]. Moreover, the low band gap value of sample BiO (2.4 eV—the lowest of the array studied here) means that it is able to utilize more energy of the irradiance source used. Lower photocatalytic activity observed for samples BiW3–BiW5 is most likely due to the fact that increased tungsten content in the coatings results in the formation of amorphous tungsten oxide and, consequently, faster recombination of photogenerated charge.

Based on the results of the indoor assessment, only the samples that exhibited the highest MB degradation rates were selected for further tests under direct solar irradiation (namely, BiO, BiW1, BiW2, and TiO₂).

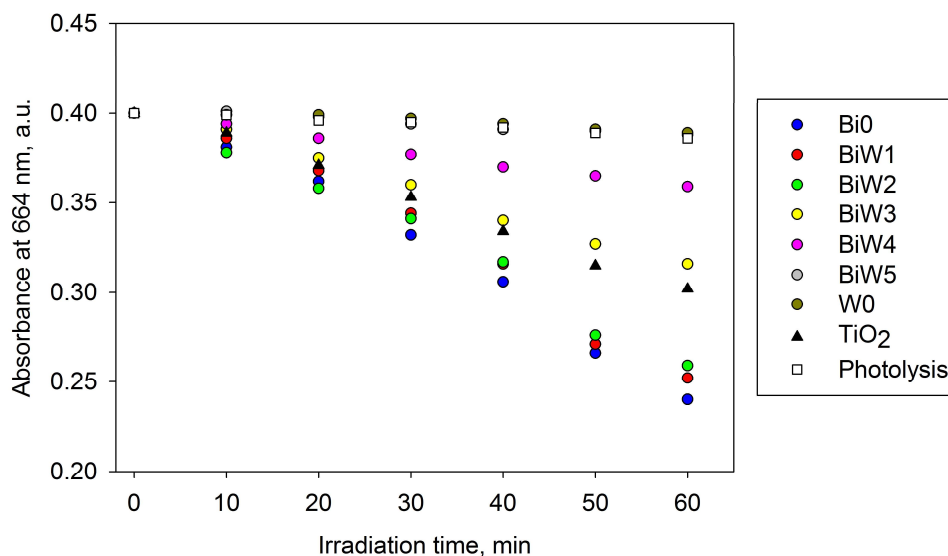


Figure 7. MB absorbance decay rates at 664 nm under fluorescent light irradiation.

2.6.2. Outdoor Assessment (Direct Solar Irradiation)

Due to the inherent variation of solar irradiance, the results of solar photocatalytic tests were compared when the global solar UV radiation reached 10 kJ L^{-1} in each round of use (Figure 8). It is noteworthy that the measurement of broadband UV radiation (200–400 nm) is considered the most appropriate spectral range to standardize photocatalytic results [34]. Results presented in the Figure 8 indicate that bismuth oxide beads (Bi0) and bismuth tungstate beads (BiW1 and BiW2) achieved considerably higher degradations of MB as compared to solar photolysis. TiO_2 coated beads showed lower activity than Bi0, BiW1, and BiW2 samples. Direct photolysis of MB solution by solar irradiation at neutral pH achieved more than 13% of degradation efficiency with 10 kJ L^{-1} of accumulated solar UV global irradiation.

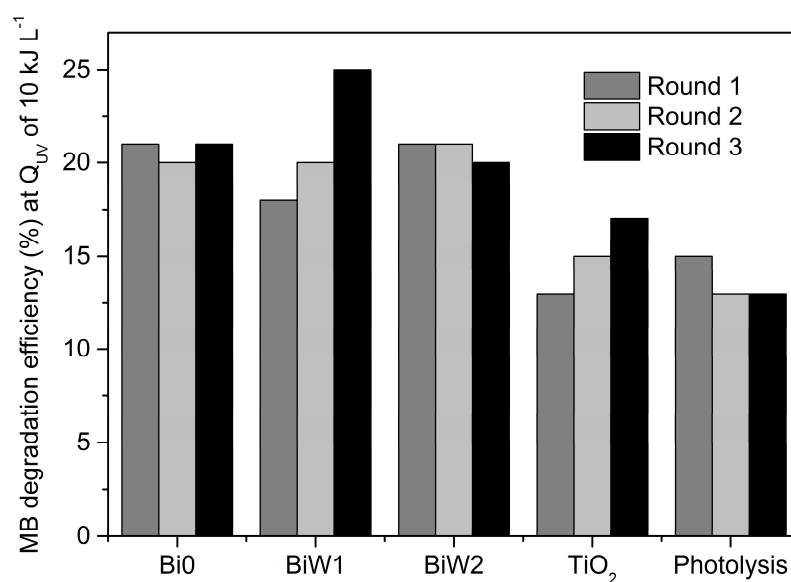


Figure 8. MB absorbance decay at 664 nm after 10 kJ L^{-1} of global accumulated UV irradiance (three rounds of use).

It is a known fact that sunlight comprises a broad spectrum of wavelengths, including IR, VIS, and UV radiation. Therefore, a global solar irradiance spectrum data was collected for each day of the photocatalytic experiments; an example of the solar spectrum (Day 1) is shown in the Figure 9. UV, VIS, and IR components were obtained via graphical integration (*Espectro* software) over the specific wavelengths range (UV: 0.28–0.40 μm ; VIS: 0.40–0.80 μm ; IR: 0.8–4.0 μm). Integration of the graph areas showed that the average solar UV irradiance was 32 W m^{-2} , the average visible irradiance— 480 W m^{-2} , the average IR irradiance— 173 W m^{-2} , while the total global solar irradiance was 685 W m^{-2} .

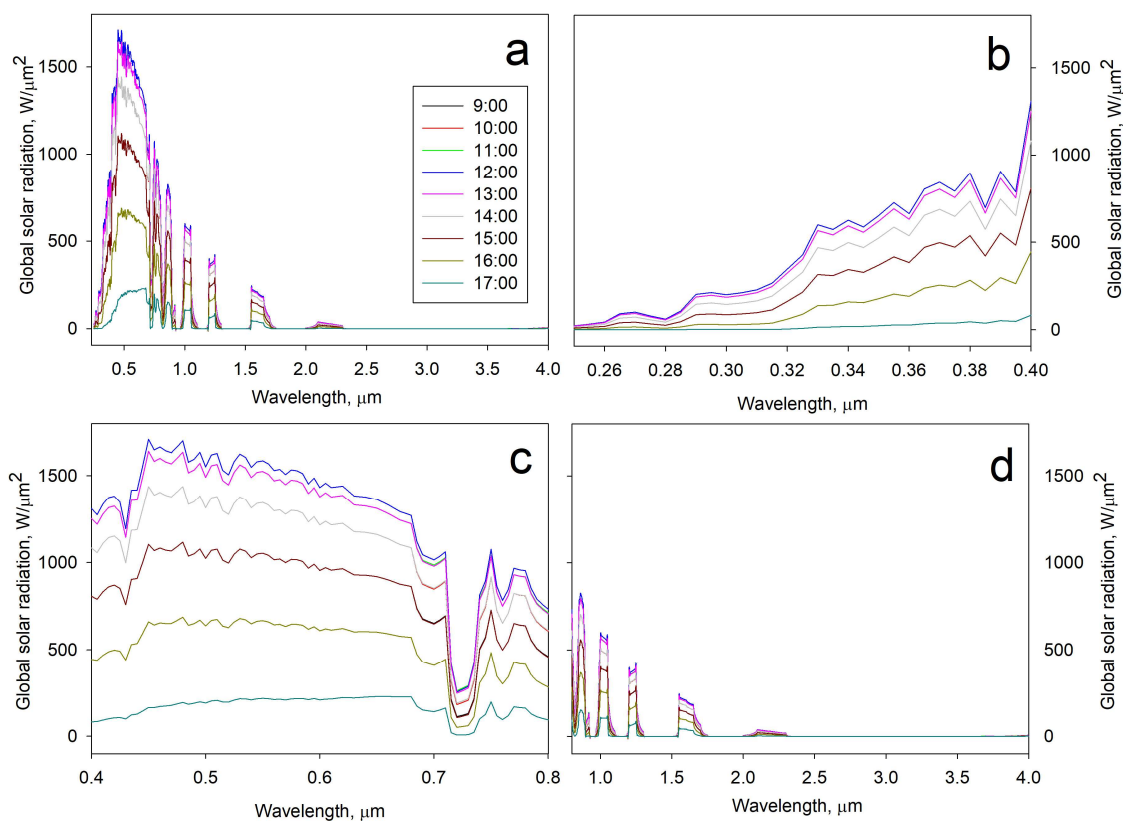


Figure 9. Example of the solar spectrum (first round of the experiments): (a) total solar irradiance; (b) the UV component of solar irradiance; (c) the visible component of solar irradiance; and (d) the IR component of solar irradiance.

Even though all three rounds of the photocatalytic experiments were performed on sunny days with similar weather conditions for the same total time (180 min), the accumulated global UV radiation varied for each experiment. Therefore, we depicted MB absorbance decay at 664 nm as a function of accumulated global (UV + VIS) irradiance; the graphs for three rounds of the experiments are given in the Figure 10.

The apparent rate constants of the reaction (k_{app}) were determined from a pseudo-first-order kinetics model from the slope of the graph of $\ln(C_0/C)$ versus time, where C_0 is the initial concentration of the solution, C is the concentration of the MB solution after 180 min of the experiment; the values of the rate constants for three rounds of the experiments are given in the Table 3.

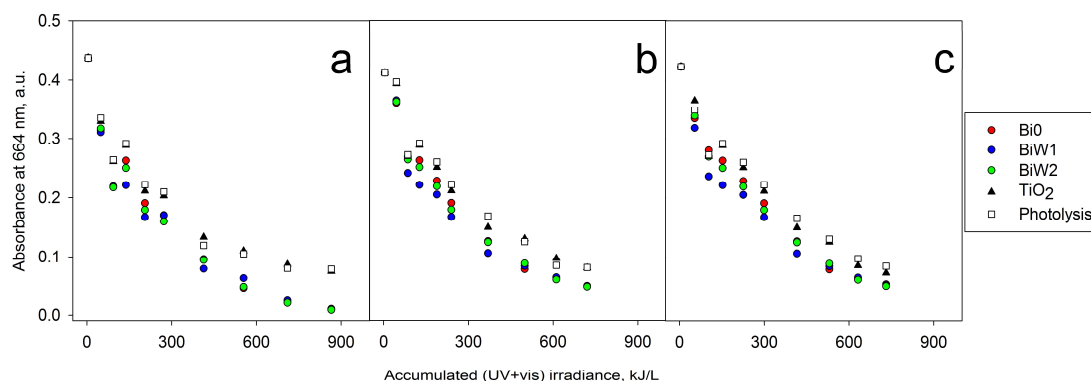


Figure 10. MB absorbance decay at 664 nm as a function of the accumulated global (UV + VIS) irradiance for three rounds of the experiments.

Table 3. Pseudo-first-order apparent constant rates (k_{app}) for methylene blue photocatalytic removal after three times of use ($R^2 \geq 0.98$).

Sample ID	Round 1 k_{app}, min^{-1}	Round 2 k_{app}, min^{-1}	Round 3 k_{app}, min^{-1}
Bi0	0.0134	0.0130	0.0103
BiW1	0.0121	0.0118	0.0101
BiW2	0.0128	0.0126	0.0103
TiO ₂	0.0085	0.0079	0.0077
Photolysis	0.0087	0.0081	0.0084

Results presented in the Table 3 show that after three rounds of photocatalyst-coated beads reuse there was a slight decrease in the apparent rate constants, however, bismuth-based materials still exhibited higher degradation rates of MB, compared to titanium dioxide-coated beads or solar photolysis.

Results show that bismuth oxide beads (Bi0) and bismuth tungstate beads BiW2 and BiW1 presented similar behavior and were all able to remove more than 90% of the MB color after the proposed solar treatment.

2.6.3. ESI-MS Study of MB Degradation

In order to identify the species produced during the methylene blue photocatalytic degradation process, the reaction products from each photocatalyst were monitored by electrospray ionization (ESI-MS). Figure 11 shows the ESI-(+)-MS spectra from the MB standard used to establish the conditions for all analyses ($m/z = 284$) (Figure 11a) and the products of the MB photocatalytic degradation in the presence of samples BiW2 and TiO₂ (Figure 11b,c, respectively). The spectra of the oxidation products show peaks at $m/z = 270, 274, 302,$ and 318 . The photocatalytic degradation in the presence of sample BiW2 (Figure 11b) catalyst resulted in a high loss of the $m/z = 284$ signal intensity, associated with MB oxidation, in correlation with the data observed by absorbance decay. Based on the other peaks observed, a methylene blue degradation pathway has been proposed (Figure 12). Thus, the pathway to the complete mineralization starts with the loss of a methyl group ($m/z = 270$, compound II). Then, there is the loss of another methylene group, and the appearance of an OH group indicates the beginning of oxidation, thus generating the compound with $m/z = 274$ (compound III). The complete degradation happens through successive oxidations resulting in the formation of the intermediate products shown as compounds IV and V in Figure 12. From the peaks of the fragmentation products depicted in the Figure 11, it is evident that the MB degradation process was more efficient in the presence of the bismuth tungstate sample, as compared to titanium dioxide.

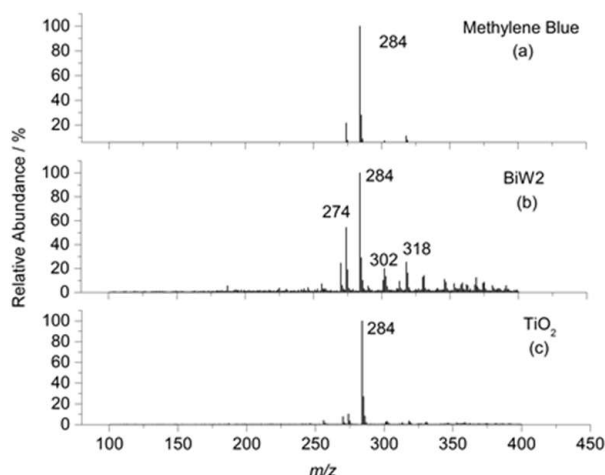


Figure 11. ESI(+)-MS: (a) methylene blue; (b) fragmentation products of MB photocatalytic degradation in the presence of the sample BiW2; and (c) fragmentation products of MB photocatalytic degradation in the presence of the sample TiO₂.

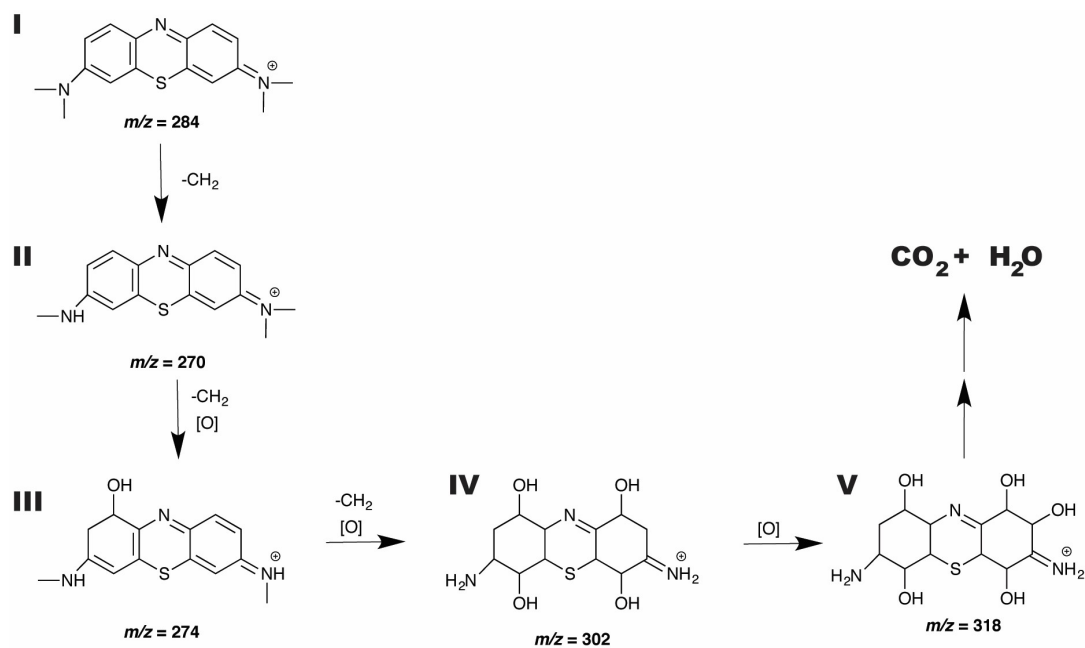


Figure 12. Schematic representation of suggested methylene blue photocatalytic degradation pathway.

Overall, it can be concluded that the results of the present work are encouraging, as it has been shown that reactive magnetron sputtered bismuth tungstate coatings possess sufficient photocatalytic properties to be used in solar-activated water treatment processes. Though the more precise optimization of the deposition conditions would be required to maximize the photocatalytic performance, it can be clearly seen that bismuth tungstate coatings have the potential to outperform titanium dioxide-based photocatalysts under direct solar irradiation, as they are able to utilize more of the solar spectrum due to their lower band gap values. More studies are being performed to confirm the performance of these materials on the degradation of contaminants of emerging concern, such as pharmaceutical and personal care products, pesticides, and illicit drugs. As it is vital that water treated with the proposed photocatalysts is safe for human consumers, toxicity studies are scheduled as a part of the follow-up work.

3. Materials and Methods

3.1. Deposition Process

Bismuth tungstate coatings were deposited in a vacuum coating system comprising two 300 mm × 100 mm planar unbalanced magnetrons (Teer Coatings Ltd., Droitwich, UK) in a closed field configuration, installed in the sputter down configuration in the top of the chamber, facing the oscillating bowl. The schematic representation of the setup is given elsewhere [20,21]. Bismuth and tungsten targets were fitted to these two magnetrons (both targets were 99.5% pure and bonded to copper backing plates). The targets were sputtered in reactive mode in a mixture of argon and oxygen. The flow of gases, introduced via mass-flow controllers, were 10 sccm of Ar and 20 sccm of O₂ for all sputtering runs. The partial gas pressure was 0.4 Pa. The magnetrons were driven in pulsed DC mode using a dual channel Advanced Energy Pinnacle Plus power supply (Advanced Energy, Fort Collins, CO, USA). A pulse frequency of 100 kHz and duty cycle of 50% (synchronous mode) were used for the deposition of all the coatings described here. The powers applied to the bismuth and tungsten targets were varied to vary the ratio of these elements in the coatings. An overview of the deposition conditions used is given in Table 1. A charge of 20 g of 2-mm round glass beads (purchased from Sigma Aldrich (Gillingham, UK) was used as a substrate; the substrates were ultrasonically pre-cleaned in propanol prior to deposition and then placed in the bowl (all reagents used at the present work were purchased from Sigma-Aldrich, unless stated otherwise). The oscillating mechanism ensures that the beads roll around the bowl, passing under each magnetron in turn. Additionally, titanium dioxide coatings were deposited onto identical glass beads for comparison purposes. Two titanium targets (99.5% pure) were used for the deposition of TiO₂ coatings; powers of 300 W were applied to each of the Ti targets in pulsed DC mode. All other deposition parameters (frequency, duty cycle, gases flow, and partial pressure) were kept the same as for the deposition of the bismuth tungstate coatings. The deposition time was 1 h for all the coatings produced in this work. All samples were post-deposition annealed in air at 673 K and then allowed to cool in air gradually (5–6 h) to avoid the formation of the thermal stresses in the coatings (the annealing temperature has been pre-defined experimentally to ensure crystallinity development for both bismuth/tungsten mixed oxide and titanium dioxide coatings).

3.2. Characterization

The composition of the coatings was investigated with EDX (EDAX Trident installed on a Zeiss Supra 40 VP-FEG-SEM, Edax Co. (Edax Co., Mahwah, NJ, USA)). Crystallographic information of the coatings was obtained with X-ray diffraction spectroscopy (Panalytical Xpert powder with CuKα1 radiation at 0.154 nm in grazing incidence mode at a 3° angle of incidence). Coating thickness was estimated with scanning electron microscopy (SEM) (Zeiss Supra 40 VP-FEG-SEM (Zeiss, Jena, Germany)). Chemical composition mapping was conducted using a FIB Quanta FEG 3D FEI microscope with a Pegasus EDS detector operated at 15 kV. The surface area and surface roughness of the coatings were determined with atomic force microscopy (AFM) (Veeco NanoScope IV MultiMode AFM (Veeco, Plainview, NY, USA)). The oxidation state information was obtained by X-ray photoelectron spectroscopy (XPS) (ThermoScientific™ ESCALAB™ 250Xi (Thermo Fisher Scientific, Waltham, MA, USA) employing an AlK source with a pass energy of 20 eV). Additionally, XPS was used for verification of the coating compositions. The optical band gap values of the coatings were calculated using the Tauc plot method [35], based on coating transmittance data. According to this method, the optical band gap of a semiconductor can be calculated using the Tauc equation by plotting $(\alpha h\nu)^{1/2}$ as a function of $h\nu$ and extrapolating the linear region to the abscissa (where α is the absorbance coefficient, h is Plank's constant, ν is the frequency of vibration). Transmittance data, used for band gap calculation, were determined using an Ocean Optics USB4000 spectrometer.

3.3. Photocatalytic Activity Assessment

Photocatalytic activity of the coated beads was assessed through the degradation of methylene blue dye using testing techniques adapted from ISO 10678:2010. MB is a blue cationic thiazine organic dye with the molecular formula $C_{16}H_{18}ClN_3S$. MB molecules contain three mesomeric structures in which the positive charge can be placed either on the amine nitrogen atom or on the sulphur atom. Aqueous solutions of MB have an intense blue colour with an absorbance peak at ca. 664 nm.

3.3.1. Laboratory Assessment (Fluorescent Irradiation Source)

An initial assessment of the photocatalytic activity was performed in the laboratory environment using a fluorescent light source (2×15 W Ushio fluorescent lamps (USHIO, Tokyo, Japan), with 64 W/m^2 total irradiance and UV component of 5 W/m^2). The emission spectrum of the light source is given elsewhere [36]. A 4 g load of the coated beads was used for each experiment; prior to the MB degradation tests the samples were immersed into 40 mL of conditioning solution of MB for 30 min in the dark with gentle magnetic stirring to reach adsorption-desorption equilibrium. The photodegradation of the MB solution was measured by monitoring the absorbance peak height at 664 nm (Ocean Optics USB4000 UV-VIS spectrometer (Ocean Optics, Dunedin, FL, USA)); the concentration of the testing solution used was $1.5 \mu\text{mol/L}$ (pre-defined experimentally to be able to detect the photocatalytic response of each sample during a 1 h initial laboratory-based assessment). Samples were immersed into 40 mL of MB test solution with continuous magnetic stirring. The full description of the testing technique used is given elsewhere. A series of reference tests was carried out to complete the evaluation of the photocatalytic activity for each sample, including tests of the coated beads in the dark, test of uncoated beads, and photolysis rate. Based on the results of the lab-based initial assessment of the photocatalytic activity, the most promising bismuth oxide-based samples were selected, tested under direct solar irradiation and compared to the performance of TiO_2 -coated beads tested under otherwise identical conditions.

3.3.2. Outdoor Assessment (Direct Solar Irradiation)

The photocatalytic activity of selected bismuth (mixed) oxide and titanium dioxide-coated beads was evaluated under direct solar irradiation in a solar magnetic stirred tank reactor. Direct solar irradiation experiments were performed on sunny days between 10:00 and 14:00 (GPS coordinates: S $19^\circ 52' 10''$, W $43^\circ 57' 40''$, 815 m—WGS84 geodetic datum). A 10 g load of the beads was used for each experiment; similarly to the laboratory-based tests, prior to the experiment the samples were immersed in the conditioning solution of MB in the dark for 30 min (concentration $10 \mu\text{mol/L}$) with continuous magnetic stirring to establish equilibrium adsorption/desorption conditions. Tests were performed using 60 mL of MB solution ($10 \mu\text{mol/L}$) for 180 min; aliquots were collected at given time intervals (0, 10, 20, 30, 45, 60, 90, 120, 150, and 180 min) for UV-VIS spectrophotometric evaluation at 664 nm (Micronal AJX-3000PC spectrophotometer (Micronal, Sao Paulo, Brazil)). The volume of the MB solution was measured and adjusted with ultrapure water hourly in order to correct the evaporation factor. All experiments were performed at room temperature (between 25°C and 29°C), with pH control.

Accumulated global UV solar irradiance was measured with a Kipp and Zonen CMP10 solar radiometer (Kipp & Zonen, Delft, Netherlands). The accumulated UV radiation (Q_{UV}) was measured and quantified (kJ L^{-1}), according to Equation (1) [34]:

$$Q_{UV} = \frac{A}{V_t} \int_0^t I_{G,UV}(t) dt \quad (1)$$

where Q_{UV} is the total accumulated incident UV radiation per litre of water solution, (kJ L^{-1}), t represents the time interval (s), $I_{G,UV}$ is the global UV irradiance (W m^{-2}), A is the irradiated area (m^2), and V_t is the total volume of treated water (L).

In order to obtain $I_{G,UV}$, the radiometer was connected to a data logger (METEON), which records incident UV radiation (W m^{-2}) during each reaction (measured at every 1 min).

Visible wavelength incident irradiation was estimated utilizing data from The Brazilian National Institute of Meteorology (INMET) automatic weather station located at Pampulha (S 19°88'39, W 43°96'94, 854 m) using *Espectro* software [37] which gives the spectral distribution of solar global radiation (including UV, VIS, and IR components). The obtained data was integrated at each desired threshold (UV, VIS, IR, and Total) and verified by comparison with UV broadband radiation measured with the radiometer previously described.

The reproducibility of the photocatalytic coatings was also tested. After each solar photodegradation reaction, the photocatalytic beads were washed with ultra-pure water and exposed to UV-C radiation (mercury vapour lamp, 80 W, Kian 4646, coated with high UV transmission glass, Schott 8405), and then reutilized with fresh MB solution and solar radiation. These steps were performed three times (three rounds of use). Kinetic data was obtained from experiments carried out in triplicate at the same solar exposure, and kinetic parameters were obtained from a pseudo-first-order kinetics model, which usually describes photocatalytic processes through the Langmuir-Hinshelwood model [37].

Intermediate chemical species of the MB degradation process were identified using mass spectrometry (MS) with an ION-TRAP LCQ Fleet (ThermoScientific, San Jose, CA, USA) in positive ion mode. Samples were analysed by direct injection into the electrospray ionization (ESI) source with a syringe pump at a flow rate of 30 L min^{-1} . Spectra were obtained as averages of 50 scans of 0.2 s each. Typical ESI conditions used a heated capillary temperature of $275 \text{ }^\circ\text{C}$, sheath gas (N_2) at a flow rate of 30 units (ca. 4 L min^{-1}) and spray voltage of 1 kV.

4. Conclusions

The present work discusses a novel technique for the reactive magnetron sputter deposition of bismuth tungstate coatings onto spherically-shaped glass beads with subsequent use of the coated beads for water treatment under direct solar irradiance. It is evident from the results that co-sputtering of bismuth and tungsten targets in an Ar/O_2 atmosphere at varied power ratios allows deposition of bismuth tungstate coatings with varied Bi/W content. This ratio has been shown to have a significant effect on the phase structure, optical properties, and photocatalytic activity of the studied coatings. The highest photocatalytic activity was achieved for the bismuth tungstate samples with a Bi/W ratio close to 2:1, which is in good agreement with previously-published data, as well as for the bismuth oxide sample. The methylene blue degradation test was chosen for evaluation of the photocatalytic properties, and the photocatalytic performance of the coated beads was initially studied indoor under fluorescent light irradiation, followed by direct solar irradiation experiments. Additionally, photocatalytic performance of Bi/W coated beads was compared to that of the beads coated with titanium dioxide, the most studied and widely used photocatalytic material. It has been shown that, due to the lower values of the band gap, bismuth tungstate coatings significantly outperformed titanium dioxide in both indoor- and outdoor-based tests.

Overall, it can be concluded that the proposed reactive magnetron sputtering technique is capable of producing uniform photocatalytic coatings onto the spherically-shaped glass beads to be used for solar light-activated water treatment applications. However, precise optimization of the deposition conditions is required in order to maximize the photocatalytic properties, as they are shown to depend greatly on the Bi/W ratio in the coatings.

Acknowledgments: The authors would like to thank the Newton Fund and CONFAP for providing funding to support the collaborative research program between Manchester Metropolitan University and Federal University of Minas Gerais (UFMG).

Author Contributions: The process design, deposition, samples characterization and writing of the first draft of the manuscript were all carried out by Marina Ratova; Rafaela Marcelino performed the photocatalytic assessment of samples under the direct solar irradiation and solar data analysis; Patterson de Souza performed the ESI-MS study of MB degradation; and Peter Kelly and Camila Amorim supervised the experimental work at the UK and Brazil sites, respectively.

Conflicts of Interest: The authors declare no conflict of interest.

References

1. Fujishima, A.; Honda, K.-I.; Kikuchi, S.-I. Photosensitized electrolytic oxidation on semiconducting n-type TiO₂ electrode. *Kogyo Kagaku Zasshi* **1969**, *72*, 108–113. [[CrossRef](#)]
2. Chen, M.; Chu, J.-W. NO_x photocatalytic degradation on active concrete road surface: from experiment to real-scale application. *J. Clean. Prod.* **2011**, *19*, 1266–1272. [[CrossRef](#)]
3. Chen, J.; Poon, C.-S. Photocatalytic construction and building materials: From fundamentals to applications. *Build. Environ.* **2009**, *44*, 1899–1906. [[CrossRef](#)]
4. Chong, M.N.; Jin, B.; Chow, C.W.K.; Saint, C. Recent developments in photocatalytic water treatment technology: A review. *Water Res.* **2010**, *44*, 2997–3027. [[CrossRef](#)] [[PubMed](#)]
5. Likodimos, V.; Dionysiou, D.D.; Falaras, P. Clean water: Water detoxification using innovative photocatalysts. *Rev. Environ. Sci. Bio/Technol.* **2010**, *9*, 87–94. [[CrossRef](#)]
6. Dong, S.; Feng, J.; Fan, M.; Pi, Y.; Hu, L.; Han, X.; Liu, M.; Sun, J.; Sun, J. Recent developments in heterogeneous photocatalytic water treatment using visible light-responsive photocatalysts: A review. *RSC Adv.* **2015**, *5*, 14610–14630. [[CrossRef](#)]
7. Wu, G.; Chen, A. Direct growth of F-doped TiO₂ particulate thin films with high photocatalytic activity for environmental applications. *J. Photochem. Photobiol. A* **2008**, *195*, 47–53. [[CrossRef](#)]
8. Han, F.; Kambala, V.S.R.; Srinivasan, M.; Rajarathnam, D.; Naidu, R. Tailored titanium dioxide photocatalysts for the degradation of organic dyes in wastewater treatment: A review. *Appl. Catal. A* **2009**, *359*, 25–40. [[CrossRef](#)]
9. Pekakis, P.A.; Xekoukoulotakis, N.P.; Mantzavinos, D. Treatment of textile dyehouse wastewater by tio2 photocatalysis. *Water Res.* **2006**, *40*, 1276–1286. [[CrossRef](#)] [[PubMed](#)]
10. Hernandez-Alonso, M.D.; Fresno, F.; Suarez, S.; Coronado, J.M. Development of alternative photocatalysts to TiO₂: Challenges and opportunities. *Energy Environ. Sci.* **2009**, *2*, 1231–1257. [[CrossRef](#)]
11. Lai, K.; Wei, W.; Zhu, Y.; Guo, M.; Dai, Y.; Huang, B. Effects of oxygen vacancy and N-doping on the electronic and photocatalytic properties of Bi₂MO₆ (M=Mo, W). *J. Solid State Chem.* **2012**, *187*, 103–108. [[CrossRef](#)]
12. Zhang, L.-W.; Wang, Y.-J.; Cheng, H.-Y.; Yao, W.-Q.; Zhu, Y.-F. Synthesis of porous Bi₂WO₆ thin films as efficient visible-light-active photocatalysts. *Adv. Mater.* **2008**, *21*, 1286–1290. [[CrossRef](#)]
13. Lin, X.; Liu, Z.; Guo, X.; Liu, C.; Zhai, H.; Wang, Q.; Chang, L. Controllable synthesis and photocatalytic activity of spherical, flower-like and nanofibrous bismuth tungstates. *Mater. Sci. Eng.* **2014**, *188*, 35–42. [[CrossRef](#)]
14. Chu, X.; Shan, G.; Chang, C.; Fu, Y.; Yue, L.; Zhu, L. Effective degradation of tetracycline by mesoporous Bi₂WO₆ under visible light irradiation. *Front. Environ. Sci. Eng.* **2016**, *10*, 211–218. [[CrossRef](#)]
15. Ratova, M.; West, G.T.; Kelly, P.J. Photocatalytic visible-light active bismuth tungstate coatings deposited by reactive magnetron sputtering. *Vacuum* **2015**, *115*, 66–69. [[CrossRef](#)]
16. Huang, Y.; Kang, S.; Yang, Y.; Qin, H.; Ni, Z.; Yang, S.; Li, X. Facile synthesis of Bi/ Bi₂WO₆ nanocomposite with enhanced photocatalytic activity under visible light. *Appl. Catal. B* **2016**, *196*, 89–99. [[CrossRef](#)]
17. Helali, S.; Polo-López, M.I.; Fernández-Ibáñez, P.; Ohtani, B.; Amano, F.; Malato, S.; Guillard, C. Solar photocatalysis: A green technology for E.Coli contaminated water disinfection. Effect of concentration and different types of suspended catalyst. *J. Photochem. Photobiol. A* **2014**, *276*, 31–40. [[CrossRef](#)]
18. Lu, X.; Peng, Y.; Han, Z. Heterogeneous photocatalytic treatment of wastewater in ultraviolet light irradiation—photocatalyst Bi₂WO₆ microsphere with high repeatability. *Front. Optoelectron.* **2012**, *5*, 439–444. [[CrossRef](#)]
19. Kelly, P.J.; Arnell, R.D. Magnetron sputtering: A review of recent developments and applications. *Vacuum* **2000**, *56*, 159–172. [[CrossRef](#)]
20. Ratova, M.; Kelly, P.; West, G.; Tosheva, L. A novel technique for the deposition of bismuth tungstate onto titania nanoparticulates for enhancing the visible light photocatalytic activity. *Coatings* **2016**, *6*, 29. [[CrossRef](#)]

21. Ratova, M.; Kelly, P.J.; West, G.T.; Tosheva, L.; Edge, M. Reactive magnetron sputtering deposition of bismuth tungstate onto titania nanoparticles for enhancing visible light photocatalytic activity. *Appl. Surf. Sci.* **2017**, *392*, 590–597. [[CrossRef](#)]
22. Zhao, G.; Liu, S.; Lu, Q.; Shi, M.; Song, L. Preparation of Bi₂WO₆ by electrospinning: Researching their synthesis mechanism and photocatalytic activity. *J. Clust. Sci.* **2011**, *22*, 621–631. [[CrossRef](#)]
23. Srikanth, B.; Goutham, R.; Badri Narayan, R.; Ramprasath, A.; Gopinath, K.P.; Sankaranarayanan, A.R. Recent advancements in supporting materials for immobilised photocatalytic applications in waste water treatment. *J. Environ. Manag.* **2017**, *200*, 60–78. [[CrossRef](#)] [[PubMed](#)]
24. Karches, M.; Morstein, M.; Rudolf von Rohr, P.; Pozzo, R.L.; Giombi, J.L.; Baltanás, M.A. Plasma-CVD-coated glass beads as photocatalyst for water decontamination. *Catal. Today* **2002**, *72*, 267–279. [[CrossRef](#)]
25. Hanaor, D.A.H.; Sorrell, C.C. Sand supported mixed-phase TiO₂ photocatalysts for water decontamination applications. *Adv. Eng. Mater.* **2014**, *16*, 248–254. [[CrossRef](#)]
26. Ratova, M.; Kelly, P.; West, G.; Xia, X.; Gao, Y. Deposition of visible light active photocatalytic bismuth molybdate thin films by reactive magnetron sputtering. *Materials* **2016**, *9*, 67. [[CrossRef](#)] [[PubMed](#)]
27. Seah, M.P.; Clifford, C.A.; Green, F.M.; Gilmore, I.S. An accurate semi-empirical equation for sputtering yields i: For argon ions. *Surf. Interface Anal.* **2005**, *37*, 444–458. [[CrossRef](#)]
28. Li, G.; Zhang, D.; Yu, J.C.; Leung, M.K.H. An efficient bismuth tungstate visible-light-driven photocatalyst for breaking down nitric oxide. *Environ. Sci. Technol.* **2010**, *44*, 4276–4281. [[CrossRef](#)] [[PubMed](#)]
29. Zhang, Y.; Zhao, Z.; Chen, J.; Cheng, L.; Chang, J.; Sheng, W.; Hu, C.; Cao, S. C-doped hollow TiO₂ spheres: In situ synthesis, controlled shell thickness, and superior visible-light photocatalytic activity. *Appl. Catal. B* **2015**, *165*, 715–722. [[CrossRef](#)]
30. Amano, F.; Nogami, K.; Ohtani, B. Enhanced photocatalytic activity of bismuth-tungsten mixed oxides for oxidative decomposition of acetaldehyde under visible light irradiation. *Catal. Commun.* **2012**, *20*, 12–16. [[CrossRef](#)]
31. Mills, A.; Hill, C.; Robertson, P.K.J. Overview of the current iso tests for photocatalytic materials. *J. Photochem. Photobiol. A* **2012**, *237*, 7–23. [[CrossRef](#)]
32. Weidong, H.; Wei, Q.; Xiaohong, W.; Xianbo, D.; Long, C.; Zhaohua, J. The photocatalytic properties of bismuth oxide films prepared through the sol-gel method. *Thin Solid Films* **2007**, *515*, 5362–5365. [[CrossRef](#)]
33. Sirota, B.; Reyes-Cuellar, J.; Kohli, P.; Wang, L.; McCarroll, M.E.; Aouadi, S.M. Bismuth oxide photocatalytic nanostructures produced by magnetron sputtering deposition. *Thin Solid Films* **2012**, *520*, 6118–6123. [[CrossRef](#)]
34. Malato, S.; Fernández-Ibáñez, P.; Maldonado, M.I.; Blanco, J.; Gernjak, W. Decontamination and disinfection of water by solar photocatalysis: Recent overview and trends. *Catal. Today* **2009**, *147*, 1–59. [[CrossRef](#)]
35. Tauc, J.; Grigorovici, R.; Vancu, A. Optical properties and electronic structure of amorphous germanium. *Phys. Status Solidi* **1966**, *15*, 627–637. [[CrossRef](#)]
36. Ratova, M.; Kelly, P.J.; West, G.T.; Iordanova, I. Enhanced properties of magnetron sputtered photocatalytic coatings via transition metal doping. *Surf. Coat. Technol.* **2013**, *228*, S544–S549. [[CrossRef](#)]
37. Laboratório de energia solar-labsol. 2017. Available online: <http://www.solar.ufrgs.br> (accessed on 20 August 2017).

